Dalton Transactions

ROYAL SOCIETY OF CHEMISTRY

PAPER

View Article Online
View Journal | View Issue

Check for updates

Cite this: *Dalton Trans.*, 2024, **53**, 656

Ion mobility mass spectrometry uncovers regioselectivity in the carboxylate-assisted C–H activation of palladium N-heterocyclic carbene complexes†

Laura Ibáñez-Ibáñez,[a] Andres Mollar-Cuni,[a] Edmond Apaloo-Messan,[b] Akhilesh K. Sharma,[b] Jose A. Mata,*[a] Feliu Maseras*[b] and Cristian Vicent*[c]

Received 28th August 2023,
Accepted 26th November 2023

DOI: 10.1039/d3dt02793g

rsc.li/dalton

Carboxylate-assisted Pd-catalyzed C–H bond activation constitutes a mild and versatile synthetic tool to efficiently and selectively cleave inert C–H bonds. Herein, we demonstrate a simple method to experimentally evaluate both reactivity and selectivity in such systems using mass spectrometry (MS) methods. The N-heterocyclic carbene (NHC) cations $[(NHC)PdX]^+$, bearing as X^- ligand bases commonly used to promote the C–H activation (carboxylates and bicarbonate), are generated in the gas-phase by ESI-MS. Their C–H bond activation at the N-bound groups of the NHC is then studied using Collision Induced Dissociation (CID) experiments. Ion Mobility Spectrometry (IM)-MS is exploited to identify a number of regioisomers associated with the distinctive site selective C–H activations. It is demonstrated that such C–H activation concomitant with acetic acid release occurs from a mixture of activated $[(NHC\text{-}H)Pd(CH_3CO_2H)]^+$ and non-activated $[(NHC)Pd(CH_3CO_2)]^+$ complexes. The identity of the X-type ligands (X = Cl^-, carboxylates and bicarbonate) has a significant impact on the regioisomer branching ratio upon CID conditions. IM-MS in conjunction with a DFT mechanistic study is presented for the acetate-assisted C–H activation of the $[(NHC)Pd(CH_3CO_2)]^+$ cation featuring butyl and aryl as N-donor groups.

Open Access Article. Published on 27 November 2023. Downloaded on 7/24/2024 11:25:06 PM.
This article is licensed under a Creative Commons Attribution-NonCommercial 3.0 Unported Licence.

Introduction

The palladium-catalyzed direct conversion of C–H into C–X (O, N, halogen, S or C) bonds constitutes a valuable method in organic synthesis.[1–5] The simultaneous combination of high reactivity and a high degree of selectivity is a prerequisite to be fulfilled by such Pd systems in order for them to be of practical importance. In particular, the use of Pd in conjunction with carboxylate salts represents a generally mild method for C–H activation.[6] It is commonly integrated into catalytic multiple-step cycles where the substrate is engaged in an initial C–H activation step, and then can react with a coupling partner.[6–8] Because these C–H activation steps are often involved in the rate-limiting step, their intimate mechanisms have been extensively investigated by experimental and computational methods and the relevance of carboxylate assistance has been clearly recognized.[9–13]

Highly regioselective carboxylate-assisted C–H activation processes can be accomplished,[14–17] particularly for ligands that contain chemical groups able to coordinate to Pd. These so-called directing groups[18] are able to bring the metal into the vicinity of a particular C–H bond. Subsequently, they undergo a ligand-directed and carboxylate-assisted C–H activation reaction commonly through cyclopalladation. N-heterocyclic carbene (NHC) ligands can be regarded as such class of ligands.[19,20] After the metalation of the imidazolium carbon atom, the NHC ligands behave as directing groups to promote C–H activation at the N-substituted groups. The relevance of cyclometallated NHC complexes in catalysis has been demonstrated.[21–24] For instance, this process is critical in the deactivation of Grubbs' second-generation olefin metathesis catalysts,[25] which in turn afford outstanding alkene isomerization cyclometallated NHC catalysts.[26] Cyclometallation at

[a]*Institute of Advanced Materials (INAM), Net of organometallic chemistry for sustainable solutions (OASIS), Universitat Jaume I, Avda. Sos Baynat s/n, 12071 Castellón, Spain. E-mail: jmata@uji.es*
[b]*Institute of Chemical Research of Catalonia (ICIQ-CERCA), The Barcelona Institute of Science and Technology, Avgda. Països Catalans, 16, 43007 Tarragona, Spain. E-mail: fmaseras@iciq.es*
[c]*Serveis Centrals d'Instrumentació Científica (SCIC). Universitat Jaume I, Avda. Sos Baynat s/n, 12071 Castellón, Spain. E-mail: barrera@uji.es*

†Electronic supplementary information (ESI) available: MS experiments, spectroscopic characterization of metal complexes and X-ray single crystal diffraction studies, energies and Cartesian coordinates of DFT optimized geometries. CCDC 2285979. For ESI and crystallographic data in CIF or other electronic format see DOI: https://doi.org/10.1039/d3dt02793g

This journal is © The Royal Society of Chemistry 2024

Open Access Article. Published on 27 November 2023. Downloaded on 7/24/2024 11:25:06 PM.
This article is licensed under a Creative Commons Attribution-NonCommercial 3.0 Unported Licence.

different N-bound groups of NHC ligands is known to afford several regioisomers that display distinctive catalytic activity,[27–30] thus being catalytic systems that are particularly appealing in the context of transition metal regiodivergent catalysis.[31] Cyclometallated NHC complexes are also intermediates *en route* to annulated NHC compounds.[32,33] The ability of promoting these annulation reactions in a regioselective fashion would imply directing the formation of regiospecific cyclometallated NHC complexes with implications also for regiodivergent catalysis. Therefore, a detailed understanding of the intimate mechanism of NHC cyclometallation is highly desirable to understand both reactivity and regioselectivity issues.

In this context, soft ionization mass spectrometry (MS) methods, such as electrospray ionization (ESI), and its tandem version are commonly used to obtain mechanistic insights in catalysis.[34–40] By using MS methods, it is possible to isolate an individual type of metal complex and directly investigate its fundamental reactivity in the gas-phase in the absence of solvents or counterions. This is illustrated through the mechanistic investigations on the gas-phase carboxylate-assisted C–H activation of phenylpyridines or acetanilides mediated by Ru, Pd and Cu.[41,42] However, regioselectivity issues cannot be directly addressed by conventional MS methods due to the inherent isobaric nature of the distinctive isomers that result from site-selective C–H bond activations. In this sense, ion mobility spectrometry mass spectrometry (IM-MS) could serve to identify these isomers as long as the site-selective C–H bond activation affords products of different topology (size and shape).[43] The use of the IM-MS technique for gas-phase ion chemistry studies was pioneered in 2011,[44,45] but mechanistic reports that rely on the use of IM-MS are still scarce.[46–52] Herein, we investigate the C–H activation at the N-bound groups of NHC palladium complexes (see Scheme 1a). Regioselectivity aspects are addressed by Ion mobility MS methods and DFT calculations.

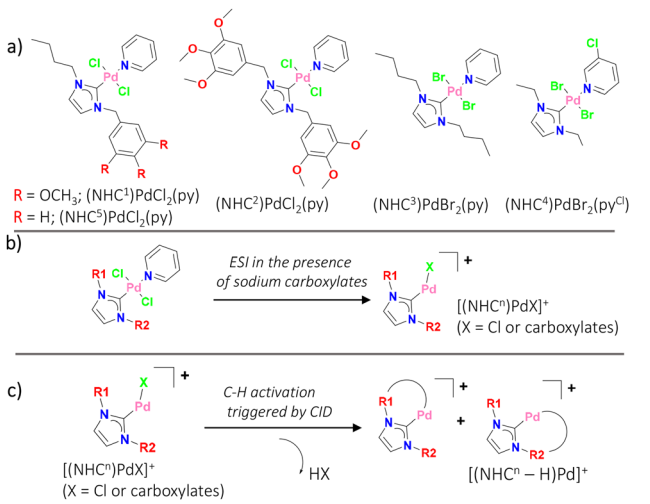

Scheme 1 NHC-Pd complexes under study (a), general ionization mode (b), and different isomers after C–H activation (c).

Results and discussion

The ESI mass spectrum of the $(NHC^1)PdCl_2(py)$ complex displayed two dominant peaks (Fig. 1). The peak attributed to the $[(NHC^1)PdCl]^+$ cation (*m*/*z* 447.1) is the base peak. It is formed through a Pd–Cl bond breaking, accompanied by the loss of the pyridine ligand. A second species is also seen formulated as $[(NHC^1 - H)Pd]^+$ (*m*/*z* 409.1), which is associated with the loss of a HCl molecule. The ^1H NMR of methanol solutions of $(NHC^1)PdCl_2(py)$ did not show evidence of either HCl or pyridine decoordination. This experimental evidence suggests that the formation of the species $[(NHC^1 - H)Pd]^+$, presumably featuring a cyclometallated NHC^1 ligand, is promoted upon the ESI conditions.

We also explored the halide ligand substitution in $(NHC^1)PdCl_2(py)$ by carboxylate (acetate and formate) and bicarbonate groups, the common bases used to promote C–H activation.[6] Such replacement can be performed readily upon ESI of methanol solutions of the $(NHC^1)PdCl_2(py)$ compound in the presence of a three-fold excess of sodium carboxylates or bicarbonate (see Scheme 1b). It resulted in a prominent peak associated with the $[(NHC^1)Pd(X)]^+$ (X = $CH_3CO_2^-$, HCO_2^- or HCO_3^-) species in their respective ESI mass spectra. The intramolecular C–H bond activation is then triggered upon CID conditions involving the second X ligand and the reactive C–H site concomitant with the liberation of HX (see Scheme 1c).

C–H activation of the $[(NHC^n)PdX]^+$ (X = $CH_3CO_2^-$, HCO_2^- or HCO_3^-) cations studied by CID-IM MS

The distinctive N-bound groups of the NHC^1 ligand, namely 3,4,5-trimethoxybenzyl and *n*-butyl, make the series of $[(NHC^1)PdX]^+$ (X = $CH_3CO_2^-$, HCO_2^- or HCO_3^-) cations amenable to trigger both C(sp^3)–H or C(sp^2)–H bond activation steps upon CID conditions. Such isomers should display differences in size and topology; thus, they could be readily differentiated by ion-mobility MS. The CID mass spectra followed by ion mobility separation of the $[(NHC^1)Pd(HCO_2)]^+$ (*m*/*z* 457.1) and $[(NHC^1)Pd(CH_3CO_2)]^+$ (*m*/*z* 471.1) cations are exemplified in Fig. 2, together with the arrival time distribution (ATD) of the product ions. The liberation of HCO_2H (Δm 46) and CH_3CO_2H

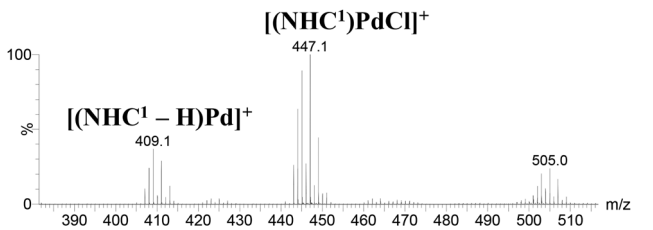

Fig. 1 ESI mass spectrum of CH_2Cl_2/methanol solutions (1×10^{-6} M) of the complex $(NHC^1)PdCl_2(py)$.

Open Access Article. Published on 27 November 2023. Downloaded on 7/24/2024 11:25:06 PM.
This article is licensed under a Creative Commons Attribution-NonCommercial 3.0 Unported Licence.

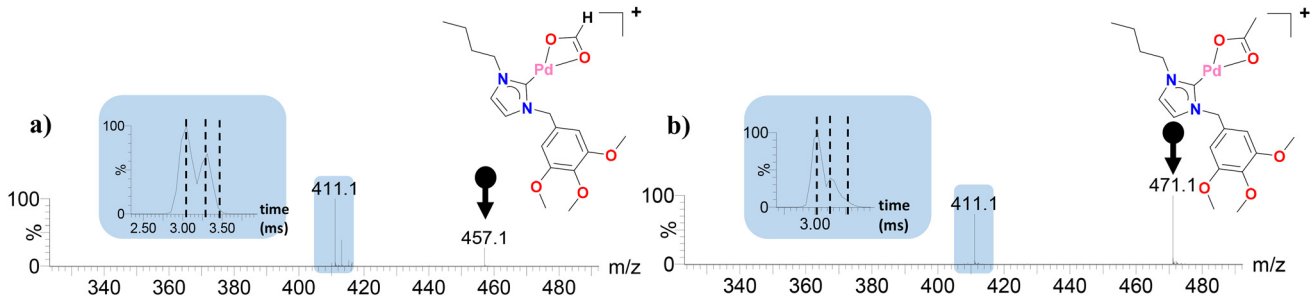

Fig. 2 CID-IM mass spectra of the precursor ions (a) $[(NHC^1)Pd(HCO_2)]^+$ (*m*/*z* 457.1) and (b) $[(NHC^1)Pd(CH_3CO_2)]^+$ (*m*/*z* 471.0) registered at a collision energy of 10 V. The insets show the ATDs of the product ions of formula $[(NHC^1 - H)Pd]^+$ (*m*/*z* 411.1) highlighting the occurrence of three mobility peaks. Note that decarboxylation (Δm = 44)[53,54] is also observed as a minor fragmentation channel for the precursor $[(NHC^1)Pd(HCO_2)]^+$.

(Δm = 60) is clearly dominant in the 2–20 V collision energy range to yield the same $[(NHC^1 - H)Pd]^+$ cation (*m*/*z* 411.1) as the sole product ion. However, the ATD of such product ion displays three mobility peaks (insets in Fig. 2) associated with the occurrence of three distinctive C–H activation sites. Two of them are prominent and centered at 3.05 and 3.25 ms, whereas a third mobility peak is barely evidenced at 3.50 ms. Likewise, the release of HCl (Δm 36) and H_2CO_3 (Δm = 62) is exclusively observed upon CID of the $[(NHC^1)PdCl]^+$ (*m*/*z* 445.1) and $[(NHC^1)Pd(HCO_3)]^+$ (*m*/*z* 473.1) cations, respectively (Fig. S2 and S3†), with a similar ATD pattern to that found for the carboxylate members.

An inspection of the ATDs of the precursor ions is also instructive. For the precursors $[(NHC^1)PdCl]^+$ and $[(NHC^1)Pd(HCO_2)]^+$, a single Gaussian-shaped mobility peak is observed at the covered collision energies. However, the ATD profiles of the precursor $[(NHC^1)Pd(HCO_3)]^+$ and $[(NHC^1)Pd(CH_3CO_2)]^+$ displayed two and three mobility traces (see Fig. S4†). As we will address below, such observation is rationalized by considering the coexistence of both non-activated and activated Pd metal complexes of the general formula $[(NHC^1)PdX]^+$ and $[(NHC^1 - H)Pd(HX)]^+$, respectively.

The study of the fragmentation characteristics upon CID conditions of the members with the symmetrical NHC^2, NHC^3 and NHC^4 ligands is instructive to clarify the origin of the regioselectivity in the congeners with the NHC^1 ligand. The CID-IM mass spectrum of the $[(NHC^2)Pd(CH_3CO_2)]^+$ displays the exclusive liberation of CH_3CO_2H to produce the product $[(NHC^2 - H)Pd]^+$ ion that displays a single Gaussian-shaped mobility peak in its ATD (see Fig. S5†). Conversely, the CID-IM mass spectrum of $[(NHC^3)Pd(CH_3CO_2)]^+$, bearing *n*-butyl as the N-bound group, affords a product ion formulated $[(NHC^3 - H)Pd]^+$ that displays two mobility peaks that are associated with the competitive C–H activation at two different positions (see Fig. S6†). In this particular case, the CID mass spectrum also reveals the elimination of ketene (Δm = 58) and NHC backbone fragmentations.[55] We believe that C–H activation at the C1 carbon atom of the *n*-butyl groups in $[(NHC^3)Pd(CH_3CO_2)]^+$ would lead to a highly strained four-member ring, and we hypothesize that C–H activation occurs at the C2 and C3 positions forming a five- or six-membered ring. Consistent with this statement, the CID mass spectrum of the complex with the ethyl group as the N-bound group, namely $[(NHC^4)Pd(CH_3CO_2)]^+$, displays only a single-Gaussian-shaped mobility peak, thus suggesting that C–H activation at the C2 position is occurring (Fig. S7†). Overall, the CID-IM study of both NHC^2 and NHC^3 congeners indicates that one C–H activation event occurs at the 3,4,5-trimethoxybenzyl group, whereas the remaining two C–H activation sites are located at the *n*-butyl group.

Complementary CID experiments registered after the ion mobility separation, the so-called CID-IM-CID experiment,[43] were performed as a means to obtain structural information of the three mobility-resolved peaks and assign them to specific

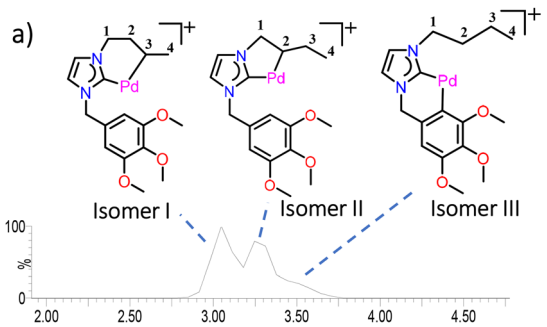

	Isomer I	Isomer II	Isomer III
Experimental[a] $^{TW}CCS_{N2}$ (Å^2)	170	174	179
Calculated CCS[b] (Å^2)	165	167	171

Fig. 3 (a) Mobility traces of the product ion $[(NHC^1 - H)Pd]^+$ formed upon CID of mass-selected $[(NHC^1)Pd(HCO_2)]^+$ together with the specific mobility peak assignment. The structures labelled as isomers **I–III** correspond to the DFT minimized geometries; (b) comparison of the experimental Collisional Cross Section of isomers **I–III** together with the calculated CCS obtained from the DFT-optimized structures. [a] $^{TW}CCS_{N2}$ refers to the determined CCS values using a Travelling Wave Ion Mobility (TWIM) instrument and nitrogen as buffer gas; [b]CCS were calculated using Trajectory Methods (TM) as implemented in the IMoS software.

This journal is © The Royal Society of Chemistry 2024

Open Access Article. Published on 27 November 2023. Downloaded on 7/24/2024 11:25:06 PM.
This article is licensed under a Creative Commons Attribution-NonCommercial 3.0 Unported Licence.

isomers. In this mode of operation, the ion mobility-resolved isomers are subjected to a second fragmentation step. A schematic picture of the mobility peak assignment is given in Fig. 3 based on CID-IM-CID and DFT calculations. The nomenclature used was isomers **I–III**, where the isomers **I** and **II** were assigned to the products resulting from C(sp^3)–H activation at the C3 and C2 position of the *n*-butyl group, whereas the isomer **III** was assigned to the product that is formed upon C(sp^2)–H activation at the aryl group, respectively. We cannot definitely rule out that C–H activation is also occurring at the C4 position. Even though seven-membered cyclometallated intermediates are less common than those with five and six-membered rings, its computed stability is similar to that of isomer **II** and its corresponding calculated Collisional Cross Section (CCS) amounts to 168 $Å^2$, so that such a hypothetic isomer **IV** would be masked by the other ones both in terms of energy and of CCS value. It is reported in the ESI,† but it will not be further discussed here.

CID-IM-CID mass spectra and a tentative assignment of the fragmentation pathways of the isomers **I–III** are shown in Fig. S8.† The CID-IM-CID mass spectra of the isomers associated with the mobility peaks at 3.05 and 3.25 ms (isomers **I** and **II**) display a product ion at *m*/*z* 229, whereas this peak is absent for the isomer attributed to the mobility peak at 3.50 ms (isomer **III**). The second-generation product ion at *m*/*z* 229 is formed through the loss of 3,4,5-trimethoxytoluene, which should be facilitated from isomers **I** and **II** *via* a single proton transfer. For the isomer **III** that is cyclometallated at the aryl group, such fragmentation should involve a complex rearrangement of the molecule, thus supporting its assignment to the mobility peak at 3.50 ms. We also note that the identity of some of the second-generation product ions of the isomers **I–III** is similar. Such similarities in the fragmentation characteristics of the ion mobility-resolved isomers point to a partial interconversion between isomer **I–III** upon CID.[56] The CID-IM-CID mass spectra of the isomers **I–III** of the $[(NHC^5 - H)Pd]^+$ cation, in which methoxo groups have been replaced by hydrogen (Fig. S9†), were also studied. The isomers **I** and **II** display a fragmentation channel associated with the elimination of toluene that is not observed for the isomer **III**. These observations suggest that releasing toluene is diagnostic of the presence of non-activated aryl N-donor groups. CID-IM-CID mass spectra of the activated $[(NHC^n - H)Pd]^+$ (n = 2–4) species were also investigated (see Fig. S10–S12†). However, they do not display any diagnostic second-generation product ions.

The specific isomer assignment was confirmed by using geometries of the three isomers obtained from computation. DFT calculations were carried out with a B3LYP-D3BJ functional in vacuum. The DFT-optimized structures were used as inputs for CCS predictions, and then these were compared with the experimental $^{TW}CCS_{N2}$ data obtained by IM-MS. From the observed drift times of the product ions, their corresponding $^{TW}CCS_{N2}$ values ($^{TW}CCS_{N2}$ refers to the determined CCS values using a Travelling Wave Ion Mobility (TWIM) instrument and nitrogen as buffer gas) were estimated by the calibration method.[57,58] The $^{TW}CCS_{N2}$values for the three isomers **I–III** were calculated using Trajectory Methods (TM), as implemented in the IMoS software.[59] The calculated structures of the cyclometallated isomers at the butyl groups, namely isomer **I** and isomer **II**, display predicted CCS values of 165 $Å^2$ and 167 $Å^2$, respectively (see Fig. 3b). These values follow the CCS trends obtained experimentally at 170 $Å^2$ and 174 $Å^2$ (for the mobility peaks at 3.05 and 3.25 ms, respectively) with CCS deviations of less than 5%. For isomer **III**, one could expect different ion topology depending on the relative conformation of the non-activated butyl group. In fact, this is an inherent issue of the Ion mobility MS analysis of molecules having flexible alkyl chains.[60] Different conformations for this isomer **III** were computationally explored to find lower energy conformers. We consider the four most stable conformers, which display energy differences of less than 1 kcal mol^{-1}, and their associated CCS values were calculated using trajectory methods. The resulting CCS values display a narrow range from 168.5 to 171.2 $Å^2$. These values support the isomer **III** cyclometallated at the aryl group displaying the largest CCS that consistently reproduces the experimental $^{TW}CCS_{N2}$ trend of 179 $Å^2$ (estimated from the mobility peak at 3.50 ms). The computed energetics will be discussed below when analyzing the reactivity, but it can already be mentioned that the most stable isomer was the one activated at the C3 position of the butyl group (isomer **I**), which in turn corresponds to the most abundant product ion observed experimentally. The isomer **I** was 7.5 and 8.5 kcal mol^{-1} more stable than those activated at the C2 position (isomer **II**) and the aryl group (isomer **III**), respectively.

The fragmentation characteristics of the member with butyl and benzyl as *N*-groups, namely $(NHC^5)PdCl_2(py)$ (see Scheme 1), are also studied. The CID-IM mass spectra of the precursor $[(NHC^5)PdCl]^+$ and $[(NHC^5)Pd(CH_3CO_2)]^+$ ions display a closely related fragmentation pattern to that found for the homologues with the (trimethoxy)benzyl group. The exclusive liberation of HCl (Δm 36) and CH_3CO_2H (Δm 60) is observed to afford up to three regioisomers (see Fig. S13 and S14†). However, their branching ratios were significantly different, with the formation of the isomer **III** (due to C(sp^2)–H activation) being more favourable.

Reactivity and regioselectivity issues

Reactivity and regioselectivity are two important characteristics of a C–H activation event. By using CID-IM experiments, these features can be evaluated in the gas-phase from the breakdown profiles of the precursor and product ions. The breakdown profiles are representations of the relative abundance of the precursor and product ions as the collision energy is increased. It is illustrated in Fig. 4 for the precursor $[(NHC^1)Pd(CH_3CO_2)]^+$ ion, and its product ions that correspond to the isomers **I–III**.

Isomer **I** is progressively formed as the collision energy is increased, and then it starts to deplete in favour of isomer **II**. As we anticipated before from the CID-IM-CID experiments of isomer **I** and **II**, this would be consistent with a possible interconversion between isomer **I** and **II**. Ion mobility MS experi-

Open Access Article. Published on 27 November 2023. Downloaded on 7/24/2024 11:25:06 PM.
This article is licensed under a Creative Commons Attribution-NonCommercial 3.0 Unported Licence.

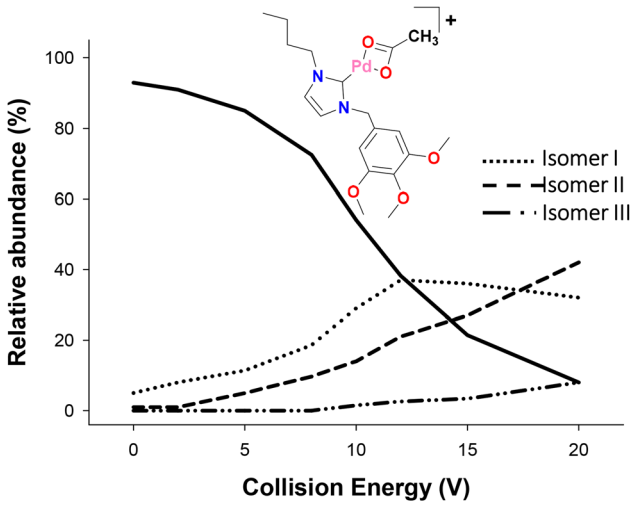

Fig. 4 Breakdown profile of the precursor $[(NHC^1)Pd(CH_3CO_2)]^+$ ion together with its product ions, namely isomer **I**–**III**. At CE values above 15 V, NHC backbone fragmentation was also evidenced to a low extent. These fragmentation channels were not drawn in the breakdown profile for clarity.

ments were exploited to study such isomerization process through the generation and mass-selection of the isomer **I** formed in the source region of the mass spectrometer, followed by CID and Ion mobility MS (Fig. 5). At low collision energy (5 V), the isomer **I** is dominant and it evolves to isomer **II** as the collision energy is raised. At a collision energy of 15 V, both isomers coexist with similar abundances. This experiment clearly indicates that such isomerization is truly occurring. Details on the energetic profiles for such isomerization are shown in Fig. S23.†

It is well-documented that switching the base on Pd catalytic systems significantly alters (or even reverses) the site selectivity of the C–H activation.[61,62] In the present case, regioselectivity can be evaluated from the branching ratios of isomers **I**–**III** extracted from the energy-resolved CID experiments (Fig. 6). The formation of isomer **I** is invariably dominant at low collision energy for all precursors with chloride, carboxylates and bicarbonate. As the fragmentation conditions are increased, ion abundances of the product associated to isomer **II** are enhanced and isomer **III** starts to form. However, in all cases, its relative abundance remains low.

Thus, for the $[(NHC^1)PdCl]^+$ cation, the regioisomer branching ratio at a collision energy of 10 V is 80/20% (isomer **I** in front of isomer **II**), while isomer **III** was not detected (Fig. 6a). At higher collision energies, the isomer **I**-to-isomer **II** branching ratio is shifted to a lower proportion of isomer **I** (65%) over isomer **II** (25%), whereas isomer **III** represents 8%. Closely related branching ratios were found for the isomers **I**–**III** generated from the $[(NHC^1)Pd(CH_3CO_2)]^+$ and $[(NHC^1)Pd(HCO_3)]^+$ precursors (Fig. 6b and c). Regioisomer branching ratio of *ca.* 60–70/40–30% at CE 10 V were observed for isomers **I** and **II**, respectively, and this trend is shifted towards an enrichment of isomer **II** and the minor formation of the isomer **III** when increasing the collision energy. The case of the $[(NHC^1)Pd(HCO_2)]^+$ cation was unique, as this species displayed a more pronounced propensity towards the formation of isomer **II**. The branching ratio is 66/34% for isomers **I** and **II**, respectively, at CE 10 V. This trend is shifted towards an isomer **II** enrichment until its ion abundance is comparable to isomer **I** at higher collision energies (Fig. 6d). Isomer **III** was, as in previous cases, barely detected only at high collision energies.

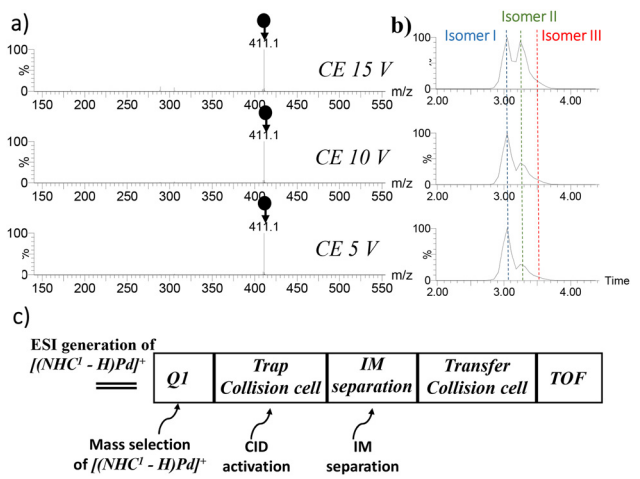

Fig. 5 (a) CID mass spectra of the mass-selected $[(NHC^1 - H)Pd]^+$ (*m*/*z* 411.1) cation at increasing collision energies, followed by IM-MS and (b) its corresponding mobility traces. The $[(NHC^1 - H)Pd]^+$ (*m*/*z* 411.1) cation was generated in the ESI source region of the mass spectrometers according to the scheme depicted in (c).

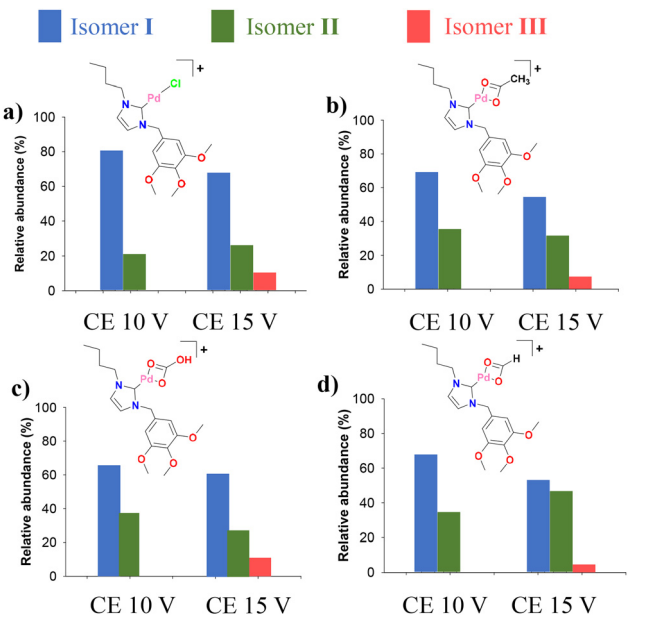

Fig. 6 Relative branching ratios of isomers **I**–**III** formed from the precursors (a) $[(NHC^1)PdCl]^+$, (b) $[(NHC^1)Pd(CH_3CO_2)]^+$, (c) $[(NHC^1)Pd(HCO_3)]^+$, and (d) $[(NHC^1)Pd(HCO_2)]^+$ investigated at collision energies of 10 and 15 V.

This journal is © The Royal Society of Chemistry 2024

Open Access Article. Published on 27 November 2023. Downloaded on 7/24/2024 11:25:06 PM.
This article is licensed under a Creative Commons Attribution-NonCommercial 3.0 Unported Licence.

DFT study on the mechanism of the site-selective acetate-assisted C–H activation

A DFT study was undertaken for the $[(NHC^1)Pd(CH_3CO_2)]^+$ cation with the NHC^1 and acetate ligand to gain insight into the competing acetate-assisted C–H activation reactions. The initial structure for this cation is depicted in Fig. 7, and displays the characteristic monodentate NHC ligand together with a bidentate acetate ligand. Fig. 7 also shows the computed free energy profile for the competing acetate-assisted C–H activation reactions at the butyl and the aryl groups. The three C–H activation processes follow a similar template. A sizeable energy barrier (27.4, 29.1, 22.4 kcal mol^{-1} for **TS1**, **TS2**, **TS3**, respectively) is overcome, and an adduct where the acetic acid fragment remains attached to the palladium centre is reached. This adduct then evolves to the three possible products, isomers **I**, **II** and **III**, through a mostly barrierless separation of acetic acid. The benzylic C–H activation is less likely, considering the higher barrier (**TS5**) and higher energy of the corresponding minima (Fig. 7 and see Fig. S22† for the energy profiles of all probable C–H activations).

In agreement with the experimental observation that cyclometallation is already occurring upon ESI conditions, we hypothesize that the ion population of the precursor ion generated by ESI indeed comprises both the non-activated $[(NHC^1)Pd(CH_3CO_2)]^+$ and the activated $[(NHC^1 - H)Pd(CH_3CO_2H)]^+$ precursors (hereafter named [isomer **I–III** + $CH_3CO_2H]^+$). This is supported by inspection of the ATD's of the precursor $[(NHC^1)Pd(CH_3CO_2)]^+$ ion (Fig. S4c†). Its ATD featured two well-resolved mobility peaks, thus pointing that several isomers constitute the ion population of the precursor ion generated by ESI. Likewise, the precursor $[(NHC^1)Pd(HCO_3)]^+$ also displayed a broad non-Gaussian mobility peak, where up to three mobility peaks were identified (Fig. S4d†). A closely related scenario was claimed recently by Roithova's group to explain the ease of the acetic acid liberation associated with C–H activation in Pd complexes bearing 2-phenylpyridine (L) by MS methods.[41] It was proposed to start either from the activated complex $[(L - H)M(CH_3CO_2H)]^+$ or the result of C–H activation in the non-activated complex $[(L)M(CH_3CO_2)]^+$, with the former being significantly favoured. In the present case, energy differences between the activated [isomer **I–III** +

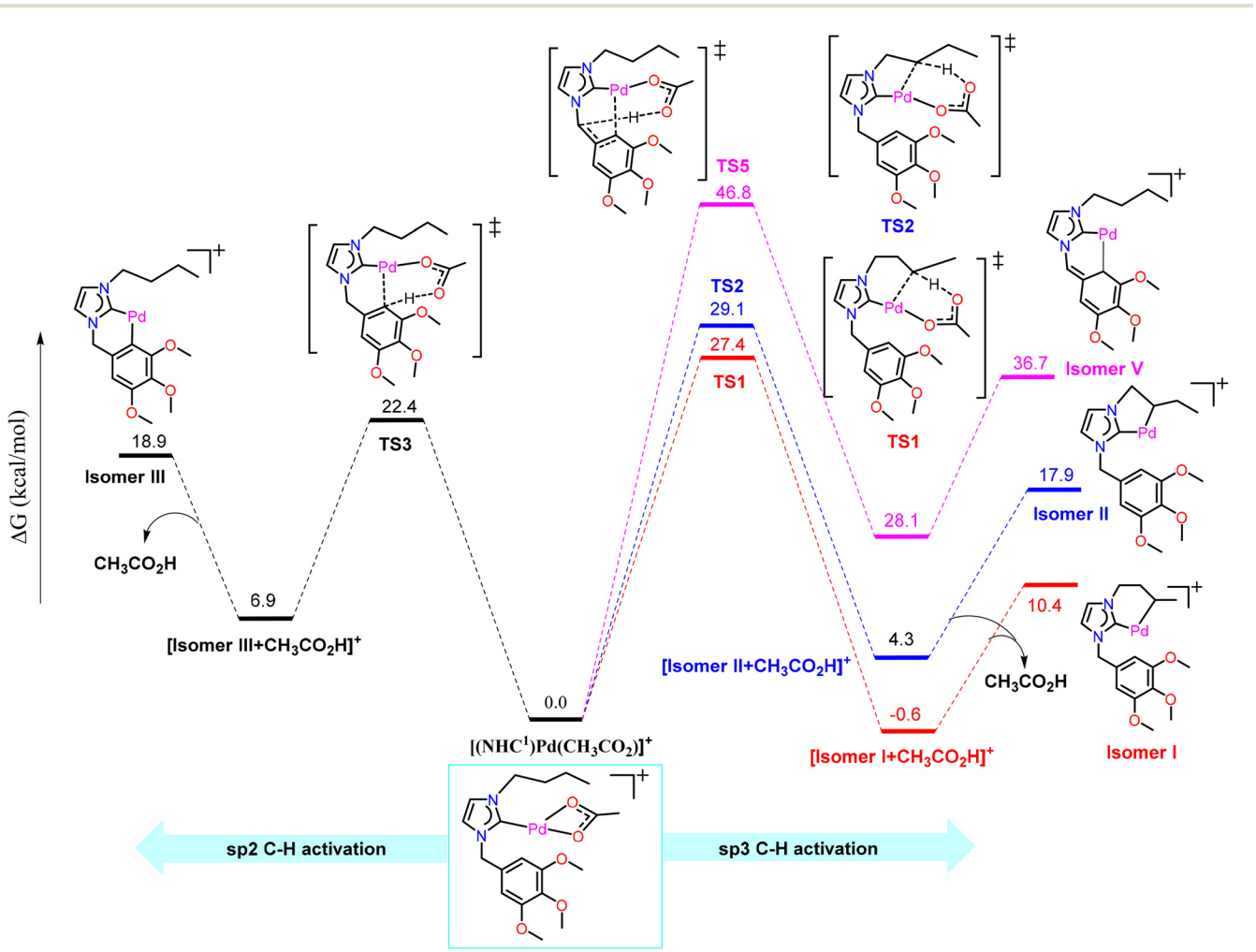

Fig. 7 Computed free energy profile (kcal mol^{-1}) for C–H activation from $[(NHC^1)Pd(CH_3CO_2)]^+$ assuming a temperature of 298 K.

Open Access Article. Published on 27 November 2023. Downloaded on 7/24/2024 11:25:06 PM.
This article is licensed under a Creative Commons Attribution-NonCommercial 3.0 Unported Licence.

$CH_3CO_2H]^+$ isomers amount to −0.6, 4.8 and 6.9 kcal mol^{-1} for the [isomer **I** + $CH_3CO_2H]^+$, [isomer **II** + $CH_3CO_2H]^+$ and [isomer **III** + $CH_3CO_2H]^+$ isomers, respectively. The thermodynamic data, therefore, suggest a major participation of [isomer **I** + $CH_3CO_2H]^+$ isomer in the sampled precursor ion population, whereas the contribution of [isomer **II** + $CH_3CO_2H]^+$ and [isomer **III** + $CH_3CO_2H]^+$ isomers should be minor. Our computed free energy profile indicates that the formation of the corresponding product ions due to the loss of acetic acid, namely isomer **I** (10.4 kcal mol^{-1}), isomer **II** (17.9 kcal mol^{-1}) and isomer **III** (19.6 kcal mol^{-1}), is associated to barrierless steps. This is consistent with our experimental isomer abundance distribution upon CID conditions.

Conclusions

The C–H bond activation of the $[(NHC^1)PdX]^+$ (X = Cl^-, carboxylates and bicarbonate) cations in the gas-phase is characterized by the formation of the sole $[(NHC^1 - H)Pd]^+$ product ion. It displays three distinctive mobility peaks in their respective CID-IM mass spectra associated with three regioselective C–H activation steps. Such C–H activations concomitant with acetic acid release occur from a mixture of activated $[(NHC\ –H)Pd(CH_3CO_2H)]^+$ and non-activated $[(NHC)Pd(CH_3CO_2)]^+$ complexes. The fragmentation channel expelling CO_2 (Δm = 44) was only observed for the $[(NHC^1)Pd(HCO_2)]^+$ member to a low extent, thus reinforcing the propensity of the investigated Pd/carboxylate (and bicarbonate) complexes to undergo C–H activation. The assignment of the mobility peaks to the specific isomers was carried out by (i) the study of palladium complexes containing different symmetric NHC ligands, (ii) CID-IM-CID experiments, and (iii) DFT calculations and comparison of experimental-*vs.*-predicted CCS values from the minimized DFT structures. Two C–H activation steps occur at the *n*-butyl group that are observed as low-energy processes. The one involving the formation of a six-membered metallacycle (C3 position, isomer **I**) of the *n*-butyl group is favoured over that forming a five-membered metallacycle (occurring at the C2, isomer **II**). Moreover, we can distinguish a unique dual origin for formation of isomer **II**. On one side, there is the direct C–H activation at the C2 site in which the precursor $[(NHC^1)PdX]^+$ itself evolves to the isomer **II**. On the other side, there is an isomerization process from isomer **I** to isomer **II**. We experimentally proved such isomerization process decoupled from the direct C–H activation *via* Ion mobility MS. In parallel, C–H activation at the aryl group is only observed at elevated collision energies for the members with the NHC^1 ligand. However, the replacement of the methoxo groups by hydrogen in the aryl groups (NHC^5 ligand) produces a major reverse of regioselectivity. In particular, the activation of $C(sp^2)$–H *versus* $C(sp^3)$–H bonds is comparable. Such insights may have implications for the regioselective synthesis of cyclometalated members, as the presence of methoxo groups in the aryl group inhibits the $C(sp^2)$–H bond activation, thus facilitating the selective formation of $C(sp^3)$–H bond activation products.

The breakdown profiles of the $[(NHC^1)PdX]^+$ (X = Cl^-, carboxylates and bicarbonate) species allowed us to explore regioselectivity aspects and identify distinctive isomer branching ratio distributions for the congeners with (X = Cl^-, carboxylates and bicarbonate). Together with the well-documented application of ESI-MS and its tandem version for mechanistic studies, we demonstrate in this work that IM-MS techniques could have an important impact in mechanistic or speciation studies in catalysis based on MS methods. For example, a commonly found challenge in MS-based mechanistic studies relies on whether the reaction product of two reactive species comprise merely an adduct formation or a genuine reaction. This is illustrated by several crucial reactions in organometallic chemistry, such as oxidative additions-*vs.*-adduct formation,[63] or inner-*vs.*-outer sphere mechanisms,[64] with most of them integrated in important transformations.

Experimental section

Materials and methods

PolyAlanine was purchased from Sigma Aldrich. The NHC complexes used in this study were synthesized as previously reported. Compound $(NHC^1)PdCl_2(py)$ was synthesized as previously reported.[65] Compounds $(NHC^2)PdCl_2(py)$ and $(NHC^5)PdCl_2(py)$ were prepared by adapting the reported method in the literature (see ESI†).[65] The synthesis of $(NHC^3)PdBr_2(py)$ and $(NHC^4)PdBr_2(py^{Cl})$ is also described in the ESI section,† along with their ^1H, $^{13}C\{^1H\}$, ESI-MS and single-crystal X-ray diffraction studies.

ESI ion mobility spectrometry mass spectrometry (ESI-IM-MS)

Experiments were performed using a SYNAPT XS High-Definition Mass Spectrometer (Waters Corporation, Manchester, UK) equipped with an electrospray ionization (ESI) source. A schematic view is given in Scheme S1.† Details on the conditions for the ESI-MS, IM-MS and CID-IM acquisitions are also given in the ESI.† Dichloromethane sample solutions (*ca.* 10^{-3} M) of the NHC complex of interest were diluted with methanol to a final concentration of 10^{-6} M, and investigated by ESI-MS and ESI-CID-IM-MS. In all compounds depicted in Scheme 1, cyclometallation was already occurring upon ESI conditions, as evidenced by the presence of prominent species of formula $[NHC^n - (H)Pd]^+$ in their respective ESI mass spectra. For the study of the carboxylate (and bicarbonate) homologues, the use of alkylammonium carboxylate salts (from acetic or formic acid and alkylamines) was detrimental at detecting cationic carboxylate-substituted Pd species in their respective positive ESI mass spectra because of the strong signal of the alkylammonium cations. Conversely, the addition of a three-fold excess of sodium carboxylate (or bicarbonate) salts to the 10^{-6} M methanol solutions of the NHC complex of interest produce prominent species in their ESI mass spectra assigned to carboxylate-substituted Pd species. For the CID-IM MS experiments, the cation of interest was mass-selected with the first quadrupole using an isolation

 This journal is © The Royal Society of Chemistry 2024

Open Access Article. Published on 27 November 2023. Downloaded on 7/24/2024 11:25:06 PM.
This article is licensed under a Creative Commons Attribution-NonCommercial 3.0 Unported Licence.

width of 1 Da, and interacted with argon in the trap region (prior to the Ion mobility separation, see Scheme S2†) by increasing the applied voltage in the trap (U_{trap}) and monitoring the Arrival Time Distribution (ATD) profiles of the product ions, while analyzing the ionic fragments with the TOF analyzer. The collision energy in the trap region (U_{trap}) was systematically increased in the U_{trap} = 2–20 V range (3 V increments), where the cyclometallation concomitant with the HX liberation was dominant. Such collision energies are not related to an absolute energy scale. At higher collision energies, complex fragmentation of the NHC backbone was observed.[55] Even at the lowest CE, partial dissociation of the precursor ion *via* HX liberation was observed in some cases. It was attributed to the loosely bound nature of the HX molecule in the precursor ion, as well as the intrinsic ion heating of the IM separation process.[66,67] For example, the extent of fragmentation for the $[(NHC^1)PdCl]^+$ precursor ion at parity of collision energy is slightly larger upon CID-IM than CID conditions. Additional experiments were performed in the transfer cell (behind the ion mobility section) by increasing the applied voltage in the transfer ($U_{transfer}$), the so-called CID-IM-CID, which aimed to prove the additional fragmentation of the previously ion mobility-resolved product ion.

The breakdown profile graphics represent the relative abundance of the precursor and product ions as the collision energy is increased. For these representations, the relative abundance of the precursor ion was calculated as $I_p/(I_p + \Sigma I_{frag})$, where I_p is the peak intensity of the precursor ion, and ΣI_{frag} is the sum of the peak intensities corresponding to all fragments. Breakdown profile representations were estimated for the series of closely related $[(NHC^1)PdX]^+$ (X = Cl, HCO_2^-, HCO_3^- and $CH_3CO_2^-$) cations. In some cases, several isomers contribute to the ion population of this product ion, and the branching ratio of each one was extracted from the deconvoluted areas of their mobility peaks from the ATD profiles according to Russell's procedure.[68] Their relative abundances from CID experiments were determined from mass spectra averaged over 80 scans. There was little variation (max. 3%) in the relative product ion abundances from three consecutive CID-IM mass spectra.

CCS calibration

Drift times were converted into CCS following the CCS calibration protocol reported by Ruotolo.[57] Calibration of the IM device for determining collision cross–sectional areas from drift time measurements was performed using a mixture of polyalanine reference ions covering the transit time of the investigated ions.[58] Their $^{DT}CCS_{N2}$ values were taken from the literature (polyAlanine[69]). As the TWIMS device is operated with N_2 buffer gas, the obtained ^{TW}CCS values will be noted as $^{TW}CCS_{N2}$. Drift times (t_D) were subjected to correction for mass-dependent and mass-independent flight times according to $t'_D = t_D - C \times \frac{\sqrt{\frac{m}{z}}}{1000} - 0.9$ (C = 1.5, and the term 0.9 ms is the mass-independent time to account for the time of transit of one wave in the IM and the transfer region). The literature CCS values were converted to CCS′ according to $CCS' = \frac{CCS\sqrt{\mu}}{z}$, where μ and z stand for the reduced mass of the collision partners and the charge state, respectively. The calibration curve is represented as CCS′ as a function of t'_D using a power law,[70] $CCS' = A \times (t'_D)^B$. Constants A and B were subsequently derived from the calibration plot, and used to calculate cross-sectional areas ($^{TW}CCS_{N2}$) of unknown species from corrected drift time measurements extracted for specific m/z values from the data.

Estimation of CCS with TM methods

For Trajectory Methods (TM) calculations, IMoS 1.10 was used.[59] Atomic coordinates were exported as .xyz files from minimized energy models. For TM methods, the potentials employed are standard TM Lenard-Jones using a 4–6–12 potential. The number of rotations was 3 with 300 000 gas molecules per rotations.

Computational details

Density functional theory calculations were performed with the Gaussian 09 package.[71] The hybrid functional B3LYP[72,73] with Grimmés dispersion corrections including Becke–Johnson damping (D3BJ)[74,75] was used for all of the calculations. All calculations were performed in gas phase. For geometry optimization, the Los Alamos National Laboratory (LANL2DZ)[76] basis set with associated effective core potentials (ECP) was used for the palladium (Pd), and the 6-31G(d)[77,78] basis set was used for C, H, O and N (BS1). All of the structures were fully optimized and established as genuine minima or transition states (TS) on the appropriate potential energy surfaces. It was confirmed by the analysis of the corresponding Hessian matrices. The IRC (Intrinsic Reaction Coordinate)[79] calculations were performed for 10 steps to ensure that the TS corresponds to the desired reaction coordinate, and the final structure was further optimized to locate the corresponding reactant and product. Potential energies (single point energies) were calculated at B3LYP-D3BJ, and cc-pVTZ-PP[80] basis set with ECP28MDF effective core potentials for Pd and cc-PVTZ for other atoms;[81,82] this combination of basis set is denoted as BS2. The cc-pVTZ-PP basis set was downloaded from the Stuttgart/Cologne group website.[83] Frequency analysis enables the calculation of thermochemical corrections and free energy correction at the BS1 basis set. The quasi-harmonic entropy correction proposed by Grimme[84] with a cutoff of 100 cm^{-1} was also employed to get free energies using GoodVibes program.[85] The conformational search[86] of isomer **III** was performed by metadynamics sampling as implemented in the xTB package[87] and using the CREST program.[88] All computational results have been uploaded to the ioChem-BD repository and can be accessed *via* https://dx.doi.org/10.19061/iochem-bd-1-297.[89]

Author contributions

The manuscript was written through contributions of all authors. All authors have given approval to the final version of the manuscript.

Open Access Article. Published on 27 November 2023. Downloaded on 7/24/2024 11:25:06 PM. This article is licensed under a Creative Commons Attribution-NonCommercial 3.0 Unported Licence.

Conflicts of interest

There are no conflicts to declare.

Acknowledgements

The authors are grateful to PID2021-126071OB-C22, PID2020-112825RB-I00, CEX2019-000925-S and RED2022-134074-T funded by MICIN/AEI/10.13039/501100011033/FEDER "Una manera de hacer Europa". Universitat Jaume I (UJI-B2022-23). L. I-I. thanks MICIN for grant (FPU20/04385). The authors thank 'Servei Central d'Instrumentació Científica (SCIC) de la Universitat Jaume I. A. K. S. thanks AGAUR for a Beatriu de Pinós fellowship (2019-BP-00190), which is co-funded by MSCA. E. A.-M. acknowledges the financial support from the European Union, under the Erasmus + Programme "Theoretical Chemistry and Computational Modelling (TCCM) and NanoX programme for the award of a mobility grant (Ecole Universitaire de Recherche, PIA3 of the Investment for the Future Program of the French Government – ANR-17-EURE-0009).

References

1 T. W. Lyons and M. S. Sanford, *Chem. Rev.*, 2010, **110**, 1147–1169.
2 T. Gensch, M. N. Hopkinson, F. Glorius and J. Wencel-Delord, *Chem. Soc. Rev.*, 2016, **45**, 2900–2936.
3 T. Rogge, N. Kaplaneris, N. Chatani, J. Kim, S. Chang, B. Punji, L. L. Schafer, D. G. Musaev, J. Wencel-Delord, C. A. Roberts, R. Sarpong, Z. E. Wilson, M. A. Brimble, M. J. Johansson and L. Ackermann, *Nat. Rev. Methods Primers*, 2021, **1**, 43.
4 L. Guillemard, N. Kaplaneris, L. Ackermann and M. J. Johansson, *Nat. Rev. Chem.*, 2021, **5**, 522–545.
5 T. Dalton, T. Faber and F. Glorius, *ACS Cent. Sci.*, 2021, **7**, 245–261.
6 L. Ackermann, *Chem. Rev.*, 2011, **111**, 1315–1345.
7 M. Albrecht, *Chem. Rev.*, 2010, **110**, 576–623.
8 J. Dupont, C. S. Consorti and J. Spencer, *Chem. Rev.*, 2005, **105**, 2527–2572.
9 D. L. Davies, S. A. Macgregor and C. L. McMullin, *Chem. Rev.*, 2017, **117**, 8649–8709.
10 B. S. Bouley, F. Tang, D. Y. Bae and L. M. Mirica, *Chem. Sci.*, 2023, **14**, 3800–3808.
11 K. M. Altus and J. A. Love, *Commun. Chem.*, 2021, **4**, 1–11.
12 Y. Boutadla, D. L. Davies, S. A. Macgregor and A. I. Poblador-Bahamonde, *Dalton Trans.*, 2009, 5820–5831.
13 A. M. Prendergast, Z. Zhang, Z. Lin and G. P. McGlacken, *Dalton Trans.*, 2018, **47**, 6049–6053.
14 D. García-Cuadrado, P. de Mendoza, A. A. C. Braga, F. Maseras and A. M. Echavarren, *J. Am. Chem. Soc.*, 2007, **129**, 6880–6886.
15 T. W. Lyons, K. L. Hull and M. S. Sanford, *J. Am. Chem. Soc.*, 2011, **133**, 4455–4464.
16 H. Choi, M. Min, Q. Peng, D. Kang, R. S. Paton and S. Hong, *Chem. Sci.*, 2016, **7**, 3900–3909.
17 V. H. M. da Silva, A. P. L. Batista, O. Navarro and A. A. C. Braga, *J. Comput. Chem.*, 2017, **38**, 2371–2377.
18 C. Sambiagio, D. Schönbauer, R. Blieck, T. Dao-Huy, G. Pototschnig, P. Schaaf, T. Wiesinger, M. F. Zia, J. Wencel-Delord, T. Besset, B. U. W. Maes and M. Schnürch, *Chem. Soc. Rev.*, 2018, **47**, 6603–6743.
19 Q. Zhao, G. Meng, S. P. Nolan and M. Szostak, *Chem. Rev.*, 2020, **120**, 1981–2048.
20 E. van Vuuren, F. P. Malan and M. Landman, *Coord. Chem. Rev.*, 2021, **430**, 213731.
21 I. Nakajima, M. Shimizu, Y. Okuda, R. Akiyama, R. Tadano, M. Nagaoka, N. Uemura, Y. Yoshida, T. Mino, H. Shinozaki and T. Yamamoto, *Adv. Synth. Catal.*, 2022, **364**, 1763–1768.
22 F. Schroeter, J. Soellner and T. Strassner, *Organometallics*, 2018, **37**, 4267–4275.
23 M. R. Chapman, C. M. Pask, A. Ariafard and C. E. Willans, *Chem. Commun.*, 2015, **51**, 5513–5515.
24 K. Wang, R. Fan, X. Wei and W. Fang, *Green Synth. Catal.*, 2022, **3**, 327–338.
25 S. H. Hong, A. Chlenov, M. W. Day and R. H. Grubbs, *Angew. Chem., Int. Ed.*, 2007, **46**, 5148–5151.
26 J. Engel, W. Smit, M. Foscato, G. Occhipinti, K. W. Törnroos and V. R. Jensen, *J. Am. Chem. Soc.*, 2017, **139**, 16609–16619.
27 A. Fizia, M. Gaffga, J. Lang, Y. Sun, G. Niedner-Schatteburg and W. R. Thiel, *Chem. – Eur. J.*, 2017, **23**, 14563–14575.
28 S. Semwal, D. Ghorai and J. Choudhury, *Organometallics*, 2014, **33**, 7118–7124.
29 G. Balamurugan, R. Ramesh and J. G. Malecki, *ChemistrySelect*, 2017, **2**, 10603–10608.
30 P. M. Illam, V. K. Singh, Priya and A. Rit, *J. Organomet. Chem.*, 2021, **951**, 122008–122017.
31 L. Ping, D. S. Chung, J. Bouffard and S. Lee, *Chem. Soc. Rev.*, 2017, **46**, 4299–4328.
32 Y. Wada, T. Takehara, T. Suzuki, S. Aoki, T. Hibi, M. Sako, H. Tsujino, Y. Tsutsumi and M. Arisawa, *Organometallics*, 2021, **40**, 2901–2908.
33 C. Dutta and J. Choudhury, *RSC Adv.*, 2018, **8**, 27881–27891.
34 J. Roithová and D. Schröder, *Chem. Rev.*, 2010, **110**, 1170–1211.
35 J. Mehara and J. Roithová, *Chem. Sci.*, 2020, **11**, 11960–11972.
36 D. Schröder, *Acc. Chem. Res.*, 2012, **45**, 1521–1532.
37 L. P. E. Yunker, R. L. Stoddard and J. S. McIndoe, *J. Mass Spectrom.*, 2014, **49**, 1–8.
38 K. L. Vikse, Z. Ahmadi and J. S. McIndoe, *Coord. Chem. Rev.*, 2014, **279**, 96–114.
39 G. J. Cheng, X. M. Zhong, Y. D. Wu and X. Zhang, *Chem. Commun.*, 2019, **55**, 12749–12764.
40 G. T. Thomas, S. Donnecke, I. C. Chagunda and J. S. McIndoe, *Chem. Methods*, 2022, **2**, e202100068.

 This journal is © The Royal Society of Chemistry 2024

Open Access Article. Published on 27 November 2023. Downloaded on 7/24/2024 11:25:06 PM. This article is licensed under a Creative Commons Attribution-NonCommercial 3.0 Unported Licence.

41 A. Gray, A. Tsybizova and J. Roithova, *Chem. Sci.*, 2015, **6**, 5544–5553.
42 J. Váňa, T. Terencio, V. Petrović, O. Tischler, Z. Novák and J. Roithová, *Organometallics*, 2017, **36**, 2072–2080.
43 A. Mollar-Cuni, L. Ibáñez-Ibáñez, G. Guisado-Barrios, J. A. Mata and C. Vicent, *J. Am. Soc. Mass Spectrom.*, 2022, **33**, 2291–2300.
44 A. Tsybizova, L. Rulíšek, D. Schröder and T. A. Rokob, *J. Phys. Chem. A*, 2013, **117**, 1171–1180.
45 L. Ducháčková, J. Roithová, P. Milko, J. Zabka, N. Tsierkezos and D. Schroder, *Inorg. Chem.*, 2011, **50**, 771–782.
46 G. J. Cheng, P. Chen, T. Y. Sun, X. Zhang, J. Q. Yu and Y. D. Wu, *Chem. – Eur. J.*, 2015, **21**, 11180–11188.
47 L. J. Song, T. Wang, X. Zhang, L. W. Chung and Y. D. Wu, *ACS Catal.*, 2017, **7**, 1361–1368.
48 C. J. Shaffer, D. Schröder, C. Gütz and A. Lützen, *Angew. Chem., Int. Ed.*, 2012, **51**, 8097–8100.
49 J.-F. Greisch, P. Weis, K. Brendle, M. M. Kappes, J. R. N. Haler, J. Far, E. De Pauw, C. Albers, S. Bay, T. Wurm, M. Rudolph, J. Schulmeister and A. S. K. Hashmi, *Organometallics*, 2018, **37**, 1493–1500.
50 R. Hilgers, S. Yong Teng, A. Briš, A. Y. Pereverzev, P. White, J. J. Jansen and J. Roithová, *Angew. Chem., Int. Ed.*, 2022, **61**, e202205720.
51 N. J. Rijs, P. González-Navarrete, M. Schlangen and H. Schwarz, *J. Am. Chem. Soc.*, 2016, **138**, 3125–3135.
52 M. Paul, E. Detmar, M. Schlangen, M. Breugst, J.-M. Neudörfl, H. Schwarz, A. Berkessel and M. Schäfer, *Chem. – Eur. J.*, 2019, **25**, 2511–2518.
53 K. L. Vikse, G. N. Khairallah, A. Ariafard, A. J. Canty and R. A. J. O'Hair, *J. Am. Chem. Soc.*, 2015, **137**, 13588–13593.
54 R. A. J. O'Hair, *Mass Spectrom. Rev.*, 2021, **40**, 782–810.
55 D. B. Eremin, D. A. Boiko, A. Y. Kostyukovich, J. V. Burykina, E. A. Denisova, M. Anania, J. Martens, G. Berden, J. Oomens, J. Roithová and V. P. Ananikov, *Chem. – Eur. J.*, 2020, **26**, 15672–15681.
56 K. Hirata, P. Chakraborty, A. Nag, S. Takano, K. Koyasu, T. Pradeep and T. Tsukuda, *J. Phys. Chem. C*, 2018, **122**, 23123–23128.
57 B. T. Ruotolo, J. L. P. Benesch, A. M. Sandercock, S.-J. Hyung and C. V. Robinson, *Nat. Protoc.*, 2008, **3**, 1139–1152.
58 V. Gabelica, A. A. Shvartsburg, C. Afonso, P. Barran, J. L. P. Benesch, C. Bleiholder, M. T. Bowers, A. Bilbao, M. F. Bush, J. L. Campbell, I. D. G. Campuzano, T. Causon, B. H. Clowers, C. S. Creaser, E. De Pauw, J. Far, F. Fernandez-Lima, J. C. Fjeldsted, K. Giles, M. Groessl, C. J. Hogan Jr., S. Hann, H. I. Kim, R. T. Kurulugama, J. C. May, J. A. McLean, K. Pagel, K. Richardson, M. E. Ridgeway, F. Rosu, F. Sobott, K. Thalassinos, S. J. Valentine and T. Wyttenbach, *Mass Spectrom. Rev.*, 2019, **38**, 291–320.
59 J. Coots, V. Gandhi, T. Onakoya, X. Chen and C. Larriba-Andaluz, *J. Aerosol Sci.*, 2020, **147**, 105570.
60 A. Ahmed, Y. Cho, K. Giles, E. Riches, J. W. Lee, H. I. Kim, C. H. Choi and S. Kim, *Anal. Chem.*, 2014, **86**, 3300–3307.
61 S. Rousseaux, M. Davi, J. Sofack-Kreutzer, C. Pierre, C. E. Kefalidis, E. Clot, K. Fagnou and O. Baudoin, *J. Am. Chem. Soc.*, 2010, **132**, 10706–10716.
62 S. R. Neufeldt and M. S. Sanford, *Acc. Chem. Res.*, 2012, **45**, 936–946.
63 K. Vikse, T. Naka, J. S. McIndoe, M. Besora and F. Maseras, *ChemCatChem*, 2013, **5**, 3604–3609.
64 C. Vicent and D. G. Gusev, *ACS Catal.*, 2016, **6**, 3301–3309.
65 A. Azua, J. A. Mata, P. Heymes, E. Peris, F. Lamaty, J. Martinez and E. Colacino, *Adv. Synth. Catal.*, 2013, **355**, 1107–1116.
66 D. Morsa, V. Gabelica and E. De Pauw, *J. Am. Soc. Mass Spectrom.*, 2014, **25**, 1384–1393.
67 C. Vicent, V. Martinez-Agramunt, V. Gandhi, C. Larriba-Andaluz, D. G. Gusev and E. Peris, *Angew. Chem., Int. Ed.*, 2021, **60**, 15412–15417.
68 C. S. Mallis, M. L. Saha, P. J. Stang and D. H. Russell, *J. Am. Soc. Mass Spectrom.*, 2019, **30**, 1654–1662.
69 M. F. Bush, I. D. G. Campuzano and C. V. Robinson, *Anal. Chem.*, 2012, **84**, 7124–7130.
70 J. P. Williams and J. H. Scrivens, *Rapid Commun. Mass Spectrom.*, 2008, **22**, 187–196.
71 Gaussian 09 Citation|Gaussian.com.
72 C. Lee, W. Yang and R. G. Parr, *Phys. Rev. B: Condens. Matter Mater. Phys.*, 1988, **37**, 785.
73 A. D. Becke, *J. Chem. Phys.*, 1993, **98**, 5648–5652.
74 S. Grimme, S. Ehrlich and L. Goerigk, *J. Comput. Chem.*, 2011, **32**, 1456–1465.
75 S. Tsuzuki and T. Uchimaru, *Phys. Chem. Chem. Phys.*, 2020, **22**, 22508–22519.
76 P. J. Hay and W. R. Wadt, *J. Chem. Phys.*, 1985, **82**, 299–310.
77 W. J. Hehre, R. Ditchfield and J. A. Pople, *J. Chem. Phys.*, 1972, **56**, 2257–2261.
78 P. C. Hariharan and J. A. Pople, *Theor. Chim. Acta*, 1973, **28**, 213–222.
79 K. Fukui, *Acc. Chem. Res.*, 1981, **14**, 363–368.
80 K. A. Peterson, D. Figgen, M. Dolg and H. Stoll, *J. Chem. Phys.*, 2007, **126**, 124101.
81 T. H. Dunning, *J. Chem. Phys.*, 1989, **90**, 1007–1023.
82 E. R. Davidson, *Chem. Phys. Lett.*, 1996, **260**, 514–518.
83 Institute for Theoretical Chemistry.
84 S. Grimme, *Chem. – Eur. J.*, 2012, **18**, 9955–9964.
85 G. Luchini, J. V. Alegre-Requena, I. Funes-Ardoiz and R. S. Paton, *F1000Research*, 2020, **9**, 291.
86 M. Besora, A. A. C. Braga, G. Ujaque, F. Maseras and A. Lledós, *Theor. Chem. Acc.*, 2011, **128**, 639–646.
87 S. Grimme, C. Bannwarth and P. Shushkov, *J. Chem. Theory Comput.*, 2017, **13**, 1989–2009.
88 P. Pracht, F. Bohle and S. Grimme, *Phys. Chem. Chem. Phys.*, 2020, **22**, 7169–7192.
89 M. Álvarez-Moreno, C. de Graaf, N. López, F. Maseras, J. M. Poblet and C. Bo, *J. Chem. Inf. Model.*, 2015, **55**, 95–103.